Electrochemical Characterization of Graphene–$LiMn_2O_4$ Composite Cathode Material for Aqueous Rechargeable Lithium Batteries

K.C. Mahesh[a*], G.S. Suresh[b]

a. Department of Chemistry, Mount Carmel College, Autonomous, Bengaluru-560052, India.
b. Department of Chemistry and Research Centre, N.M.K.R.V. College for Women, Bengaluru-560 011, India.

Abstract

A series of graphene– $LiMn_2O_4$ composite electrodes were prepared by physical mixing of graphene powder and $LiMn_2O_4$ cathode material. $LiMn_2O_4$ was synthesized by reactions under autogenic pressure at elevated temperature method. CV, galvanostatic charge-discharge experiments and EIS studies revealed that the addition of graphene significantly decreases the charge-transfer resistance of $LiMn_2O_4$ electrodes. 5 wt. % graphene–$LiMn_2O_4$ composite electrode exhibits better electrochemical performance by increasing the reaction reversibility and capacity compared to that of the pristine $LiMn_2O_4$ electrode. Improved electrochemical performances are thus achieved, owing to the synergic effect between graphene and the $LiMn_2O_4$ active nanoparticles. The ultrathin flexible graphene layers can provide a support for anchoring well-dispersed active cathode particles and work as a highly conductive matrix for enabling good contact between them. At the same time, the anchoring of active nanoparticles on graphene effectively reduces the degree of restacking of graphene sheets and consequently keeps a highly active surface area which increases the lithium storage capacity and cycling performance.

Key words: Li-ion batteries, Graphene–$LiMn_2O_4$ composite electrodes, Cyclic voltammetry, Galvanostatic charge-discharge experiments, EIS studies

---

* Author for correspondence
Telephone: +91-80-22261759
Fax: +91-80-22286386
E-mail address: kcmahesh78@hotmail.com (K.C. Mahesh)

1. Introduction

Lithium manganese oxide ($LiMn_2O_4$) with the cubic-spinel structure (the term *spinel* formally refers to the mineral $MgAl_2O_4$, although the term is used for materials with equivalent structure) is one of the most widely researched cathode materials for lithium secondary batteries because of their low cost, abundance, and low toxicity, relatively high energy density, easy synthetic process, and higher voltages than currently commercialized $LiCoO_2$ [1]. The battery system based on $LiMn_2O_4$ as positive electrode has been used commercially in many types of electronic equipment with carbon as the negative electrode [2]. However, the capacity fading of $LiMn_2O_4$ upon cycling particularly above 40 °C is one of the drawbacks that need to be improved for a wide use of $LiMn_2O_4$ as cathode material in rechargeable lithium batteries. The reason behind the capacity loss during cycling is not identified clearly yet, and several possible causes are suggested, such as an instability of the organic based electrolyte at high charge potential [3], the slow dissolution of manganese into the electrolyte [4], Jahn-Teller distortion [5], change in crystal lattice arrangement with cycling [6], site exchange between lithium and manganese [7], particle disruption of parent particle [8], and so on.

Applying the concept of the cooperative Jahn-Teller distortion, several investigations have been made to overcome capacity fading by doping the spinel with other metal cations such as cobalt [9], nickel [10], chromium [11], iron [12], aluminium [13], and magnesium [14]. It was expected that replacing part of the manganese with another metal could increase the stability of the spinel structure and improve the cycling performance of Mn spinel when it is employed as the cathode material. Materials with ad metal content offer improved storage stability in the discharged state as manganese disproportionation is inhibited when the Mn^{3+}: Mn^{4+} ratio is reduced.

Further research was carried out to identify new additives, which would improve the cycling stability of $LiMn_2O_4$ material. Electronically conducting polymers such as polypyrrole, polyaniline and polythiophene have attracted attention as electrodes in batteries [15, 16]. Apart from being electrochemically active, they also act as conducting additive, thereby reducing the inert weight associated in the preparation of the electrode. The incorporation of these polymers in the cathode materials increases the conductivity and thus improves the high-rate discharge behavior.

The electrochemical performance of various electrode materials can be significantly boosted by rendering them conducting with graphene sheets [17-19]. In the family of carbon nanostructures, graphene is the youngest member but has attracted enormous recent interest. Graphene is a two-dimensional macromolecular sheet of carbon atoms with a honeycomb structure. It is an excellent substrate to host active nanomaterials for lithium-ion battery applications due to its high conductivity, large surface area, flexibility, and chemical stability. In this regard, chemically modified graphene materials have been used to form the heterogeneous nanostructured materials with Si [20], SnO_2 [21], Co_3O_4 [22] etc. Improved electrochemical performances are thus achieved, owing to the synergic effect between graphene and active nanoparticles. In these nanocomposites, the ultrathin flexible graphene layers can provide a support for anchoring well-dispersed active nanoparticles and work as a highly conductive matrix for enabling good contact between them, which can also effectively prevent the volume expansion/contraction and aggregation of the active nanoparticles during lithium charge/discharge processes. Meanwhile, the anchoring of active nanoparticles on graphene effectively reduces the degree of restacking of graphene sheets and consequently keeps a highly active surface area and to some extent, increases the lithium storage capacity and cycling performance.

Though graphene sheets can effectively buffer the strain from the volume change of metals or metal oxides during the charge/discharge processes and preserve the high electrical conductivity of the overall electrode, the metal and metal oxide nanoparticles are still prone to strong aggregation during the cycling processes because of non-intimate contact between graphene layers and active nanoparticles, leading to a slow capacity fading. An alternative strategy for solving the aggregation problem of metal and metal oxides is to confine them within individual graphene shells. Yang et al. [22] reported graphene encapsulated Co_3O_4 nanoparticles prepared by co-assembly between negatively charged graphene oxide and positively charged oxide nanoparticles. This assembly enables a good encapsulation of electrochemically active metal oxide nanoparticles by graphene sheets, thus leading to a remarkable lithium-storage performance such as highly reversible capacity and excellent cycling performance. A very high and stable reversible capacity was achieved for the graphene encapsulated Co_3O_4 electrode, which is superior to those of Co_3O_4/graphene composite or bare Co_3O_4 electrodes.

With an idea to improve the electrochemical properties of $LiMn_2O_4$, we prepared graphene–$LiMn_2O_4$ composite electrode using physical admixing method, and it was used as a cathode material for an aqueous rechargeable lithium battery. $LiTi_2(PO_4)_3$ and 2 M Li_2SO_4 aqueous solution were used as anode and electrolyte, respectively. Cyclic voltammetry, galvanostatic charge–discharge, and electrochemical impedance spectroscopy techniques were used to investigate the effect of graphene addition to $LiMn_2O_4$.

2. Experimental

2.1 Synthesis of Electrode Materials by RAPET (reactions under autogenic pressure at elevated temperature) Method

Stoichiometric amounts of the precursors were weighed, mixed, and then ground well. The resulting powder was pressed into pellets to improve the reactivity between the particles of the precursor and introduced into a 5 mL Swagelok cell. The Swagelok parts consist of a small threaded stainless-steel tube closed by two caps from both sides. For this synthesis, about 0.6 g of the precursors was introduced into the cell. The filled Swagelok was closed tightly in oxygen environment and then placed inside an alumina pipe in the middle of a programmable furnace. The temperature was raised at a rate of 10 °C/minute to the desired / required temperature and held for an optimized time. The details are given in **Table 1** The chemical dissociation and transformation reaction takes place under the autogenic pressure of the precursor at the fixed temperature. The Swagelok cell was allowed to cool gradually to room temperature, opened and the obtained product was used after grinding. By using this method, we obtained particles of size of about 100 nm. Details regarding the amount of the precursors and their stoichiometric calculations are given in **Table 2**.

Table 1. Summary of starting materials and synthesis conditions for electrode materials by RAPET method.

Compound	Precursors	Temperature (°C)	Time of heating (hrs)
$LiMn_2O_4$	LiOH, MnO_2	600	10
$LiTi_2(PO_4)_3$	LiH_2PO_4, TiO_2, $NH_4H_2PO_4$	900	15

Table 2. Amount of different precursors taken with the stoichiometric calculation for the synthesis of $LiMn_2O_4$ and $LiTi_2(PO_4)_3$ by RAPET method.

$LiMn_2O_4$

Precursors	**LiOH**	**MnO_2**
Mol. mass	23.95	86.94
No. of moles required	1.05	2.0
Wt. taken	**0.083 g**	**0.576 g**
		Total weight = **0.659 g**

$LiTi_2(PO_4)_3$

Precursors	**LiH_2PO_4**	**TiO_2**	**$NH_4H_2PO_4$**
Mol. Mass	103.93	79.90	115.03
No. of moles required	1.05	2.0	2.0
Wt. taken	**0.125 g**	**0.183 g**	**0.263 g**
			Total weight = **0.571 g**

2.2 Preparation of the Electrodes

Electrodes were prepared by using stainless steel mesh as a current collector. The mesh was cut into circular shape of about 1 cm^2 area and welded with stainless steel wire for electrical contact. The mesh was sand blasted to remove the oxide layer, washed with water, rinsed with acetone, dried, and weighed. Cathode and anode electrodes were prepared in the same way. Powder mixture of the sample, carbon black and polyvinylidene fluoride in the weight ratio 75:20:5 was ground in a mortar, transferred to a small sample tube made up of glass; a few drops of *N*-methyl-2-pyrrolidone were added to get a slurry and was stirred overnight with the help of a magnetic pellet. To prepare the slurry 0.4 g of the active material was taken at a time. The slurry was coated onto the pretreated mesh and dried in a vacuum oven at 110 °C overnight. $LiTi_2(PO_4)_3$ electrodes were dried for 24h at 100 °C.

2.3 Assembly of the Cell

A three-electrode electrochemical cell was employed for cyclic voltammetry, impedance measurements, potentiostatic and galvanostatic intermittent titration techniques. The prepared electrode of the cathode, a saturated calomel electrode and Pt foil were used as working, reference and counter electrodes, respectively. A small, covered beaker of about 20 mL volume was used as the cell, and contains the three electrodes (working, reference, and counter), which were immersed in the sample solution. Volume of electrolyte solution used was 10 mL. The

electrodes were inserted through holes in the cell cover. While the working electrode is the electrode at which the reaction of interest occurs, the reference electrode provides a stable and reproducible potential (independent of the sample composition), against which the potential of the working electrode is compared. Such "buffering" against potential changes is achieved by a constant composition of its redox couple, Hg/Hg_2Cl_2, with the saturated calomel reference electrode. All the electrochemical measurements were made using a Biologic potentiostat-galvanostat instrument.

3. Results and discussion

3.1 Physical characterization.

The XRD pattern of $LiMn_2O_4$ compound prepared by RAPET method at 600 °C for 10 h and is shown in **Figure 1a**. $LiMn_2O_4$ belongs to *Fd*3*m* cubic space group in which lithium ions are at the tetrahedral 8*a* sites, manganese ions at the octahedral 16*d* site, and oxygen ions at the 32*e* sites forming fcc packing arrangements [23]. The anion lattice in $LiMn_2O_4$ contains cubic close-packed oxygen ions and is closely related to the α-$NaFeO_2$ layer structure, differing only in the distribution of the cations among the available octahedral and tetrahedral sites. Mn_2O_4 framework provides three-dimensional interstitial space for lithium-ion transport maintaining its structure over the compositional range $Li_xMn_2O_4$ ($0 \leq x \leq 1$) by changing the average manganese oxidation state between 3.5 and 4 [24]. Lithium can be inserted into or extracted from $LiMn_2O_4$ by electrochemical redox reactions. The extraction of lithium from $LiMn_2O_4$ results in λ-MnO_2, while insertion produces $Li_2Mn_2O_4$. This insertion induces the Jahn-Teller distortion of Mn^{3+} ions, favoring the phase transitions from a cubic to a tetragonal structure [25]. Lee et al. [26] reported that the lithium ion occupies both the tetrahedral and octahedral sites of the spinel structure. It was shown that the materials synthesized at lower temperatures (550-650 °C) have defects in the normal spinel structure and do not undergo Jahn-Teller distortion, whereas the materials synthesized at higher temperatures (800 °C) undergo a cubic to tetragonal phase change below room temperature. The structural distortion results from interaction of the Jahn-Teller active species Mn^{3+} ($t_{2g}^3e_g^1$).

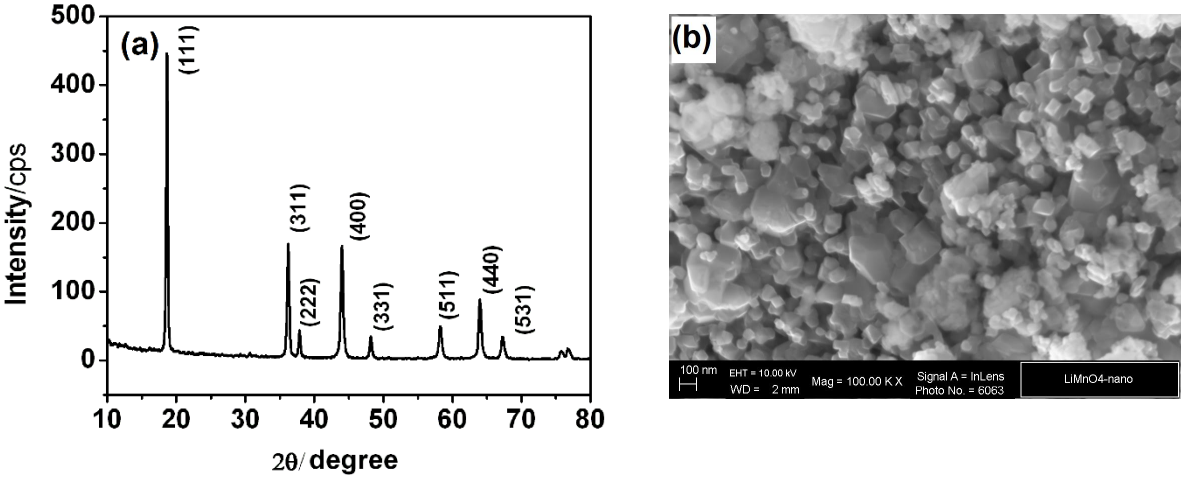

Figure 1: (a) XRD pattern and (b) SEM images of $LiMn_2O_4$ particles synthesized by RAPET method.

The XRD pattern of the sample obtained agrees with the pattern of pure cubic spinel phase of $LiMn_2O_4$ (JCPDS file No. 88-1030). The intensity ratio of (111) and (311) [or (400)] peaks is high. This indicates no pronounced cation mixing and thereby the electrochemical activity of these cathode materials in terms of capacity and rates of lithium-ion de-insertion/insertion

is to be very good. The value of lattice parameter a = 8.187 Å obtained for the sample agree well with the literature value [27]. We conclude from this XRD results that there are no remarkable impurities in the materials obtained and the ions are compatible in the cubic structure and pure phase solid solutions were obtained.

Scanning electron microscopy was used to analyze the particle size and morphology of the $LiMn_2O_4$ material prepared and is shown in **Figure 1b**. From the micrographs it can be seen that the particles are non-spherical in shape with a size of about 100 nm. The well-dispersed particles are the result of the reaction, which takes place at autogenic pressure at elevated temperature that reduces the synthesis time and shortens the particle size. Such kind of morphology is very important to both the high specific capacity and good cyclability of cathode materials.

3.2 Cyclic voltammetry.

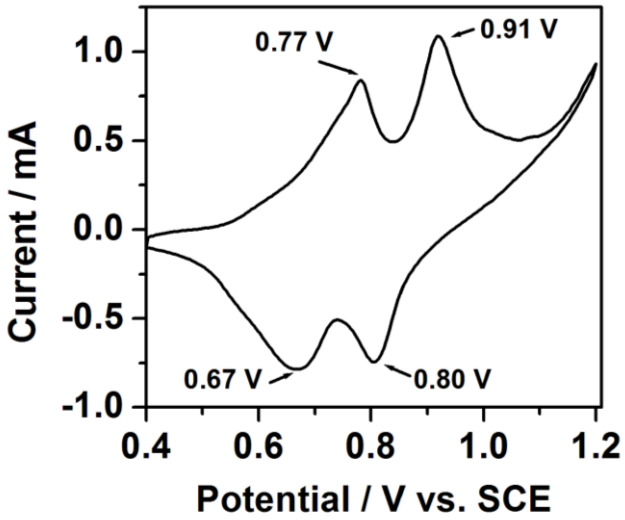

Figure 2: CV of $LiMn_2O_4$ electrode in 5 M $LiNO_3$ aqueous electrolyte prepared by RAPET method (scan rate = 0.1 mVs^{-1}).

The Cyclic voltammogram of $LiMn_2O_4$ prepared by RAPET method in 5 M $LiNO_3$ aqueous solution at a scan rate of 0.1 mV s^{-1} between 0.4 and 1.2 V using saturated calomel and Pt-foil as reference and counter electrodes, respectively is shown in **Figure 2**. $LiMn_2O_4$ shows two pairs of anodic and cathodic peaks located at 0.77/0.67 V and 0.91/0.80 V with a potential difference of 0.10 and 0.11 V, respectively, corresponding to lithium deintercalation and intercalation of $LiMn_2O_4$ electrode in accordance with the following equations.

$$\text{Deintercalation: } LiMn_2O_4 \rightarrow Li_{1-x}Mn_2O_4 + xLi^+ + xe^- \quad (1)$$

$$\text{Intercalation: } Li_{1-x}Mn_2O_4 + xLi^+ + xe^- \rightarrow Li_{1-x}Mn_2O_4 \quad (2)$$

The anodic peaks appear due to the oxidation of manganese ions accompanied by the deintercalation of equal number of lithium ions. The cathodic peaks are due to the reduction of manganese ions accompanied by the intercalation of lithium ions. During these processes, no oxygen evolution peak can be observed, which is obviously due to the over potential of the electrode. This shows that it is possible to remove lithium ions from the material before the

evolution of oxygen. Thus, it is possible to use the prepared $LiMn_2O_4$ as cathode material in the aqueous solution without much oxygen evolution.

The appearance of two peaks indicates that, lithium intercalation in $LiMn_2O_4$ takes place in two steps. In the first step (the lower potential peaks), lithium ions occupy every other available tetrahedral site (8a) in the spinel structure, until half of the sites are filled. This is in the lithium-depleted state ($0 \leq x \leq 0.5$ in $Li_xMn_2O_4$). In the second step (the higher potential peaks), lithium ions fill the remaining empty 8a sites. This is in the lithium-rich state ($0.5 \leq x \leq 1$ in $Li_xMn_2O_4$), which is different from that in the lithium-depleted state because there exists a repulsive interaction during lithium intercalation in the lithium-rich state.

In spinel $Li_xMn_2O_4$, there should exist channels and vacant sites available for lithium ions to diffuse and occupy. It is reasonable to assume that those sites distributed in the $Li_xMn_2O_4$ lattice are equivalent according to the lattice gas model with mean field approximation [28]. At the lithium-depleted state, the interactions between lithium ions can be neglected because of the greater distance from each other in the $Li_xMn_2O_4$ lattice. Lithium ions can diffuse freely through the channels and then occupy every other available tetrahedral site, forming a bond to the bridging-type oxygen. The lithium ions located at the inserted sites are immobile due to the Li–O bonds, while the incoming lithium ions diffuse through the channels and occupy the remaining vacant sites. In other words, lithium diffusion step and lithium-ion occupation step in the lattice takes place successively. In the lithium-rich state, every other insertion site has been filled with lithium ions. The incoming lithium ions have to overcome repulsive interactions with those lithium ions located at the inserted sites. For the lithium-ion diffusion channel to be available, the lithium ions located at inserted sites must hop and occupy their nearest neighbor and empty their sites, accompanied by the breakdown of old Li–O bonds and the formation of new Li–O bonds. The applied potential is responsible for the breakdown of Li–O bonds. At this state, lithium-ion diffusion and lithium-ion occupation take place simultaneously [29].

Cyclic voltammetric measurements were performed to examine the electrochemical properties of different graphene – $LiMn_2O_4$ composite electrodes. The CV profiles obtained at room temperature in the first cycle are as shown in **Figure 3**. Even though, all these voltammograms are characterized by two pairs of redox peaks, there is a pronounced difference in the behavior of different graphene – $LiMn_2O_4$ electrodes with respect to peak current and potential. The CV profile of 5 wt.% graphene – $LiMn_2O_4$ is found to exhibit more peak current and reversibility. As for cyclic voltammogram curves are considered, the potential interval between anodic peak and cathodic peak is an important parameter to evaluate the electrochemical reversibility. As shown in Figure 3, 5 wt.% graphene – $LiMn_2O_4$ composite electrode exhibited anodic responses at 0.85 and 0.98 V with 3.91 and 5.93 mA currents and the corresponding cathodic responses are at 0.81 and 0.92 V with −3.01 and – 4.66 mA currents.

The details of peak current and peak potentials for second peak pair of all compositions are summarized in **Table 3**. These results indicated that the overpotential for the deintercalation and intercalation process was reduced after admixing graphene with $LiMn_2O_4$. The well-defined peaks and smaller values of potential intervals further showed the enhancement of electrode reaction reversibility by the addition of graphene. The peak potential differences ($E_{p,a}$–$E_{p,c}$) of pristine, 2.5, 5, 7.5 and 10 wt.% graphene – $LiMn_2O_4$ electrodes at 0.1 mV s−1 scan rates are also listed in Table 3.

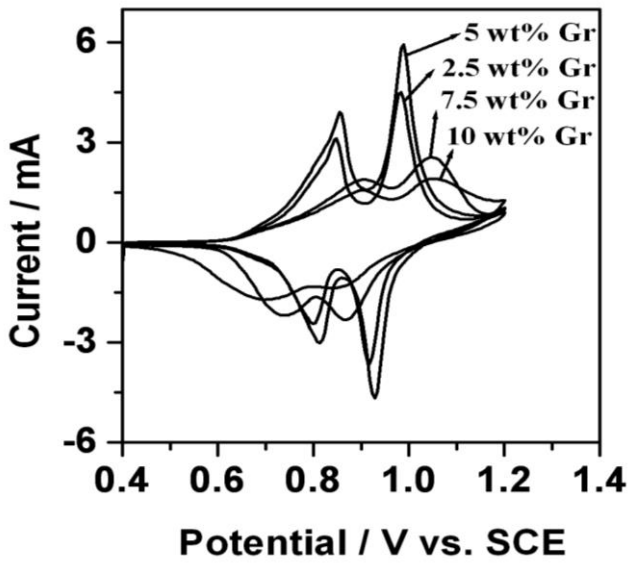

Figure 3: Cyclic voltammograms of different graphene – $LiMn_2O_4$ composite electrodes in 5 M $LiNO_3$ electrolyte with a scan rate of 0.1 mVs^{-1}.

Table 3. Peak potential, peak potential difference, and peak current for second peak pair for pristine and graphene-treated electrodes.

Composition	$E_{p,a}$ (V)	$E_{p,c}$ (V)	$E_{p,a} - E_{p,c}$ (V)	$I_{p,a}$ (mA)	$I_{p,c}$ (mA)
Pristine	0.918	0.805	0.113	1.091	−0.750
2.5 wt. % graphene	0.983	0.918	0.065	4.501	−3.625
5 wt. % graphene	0.989	0.928	0.061	5.931	−4.668
7.5 wt. % graphene	1.048	0.868	0.180	2.567	−2.310
10 wt. % graphene	1.078	0.843	0.235	1.522	−0.906

It is clear from the table that the potential interval between anodic and cathodic peaks decreases with increase in graphene percentage up to 5 wt. % and thereafter it increases again. Similarly, the anodic and cathodic peak current values show a maximum for 5 wt. % electrode. As the electrode with 5 wt. % graphene – $LiMn_2O_4$ electrode shows better voltammetric behavior, this composition was chosen for further electrochemical studies of the system under investigation. It should be noted that the electrochemical studies of other compositions show similar but poor electrochemical characteristics.

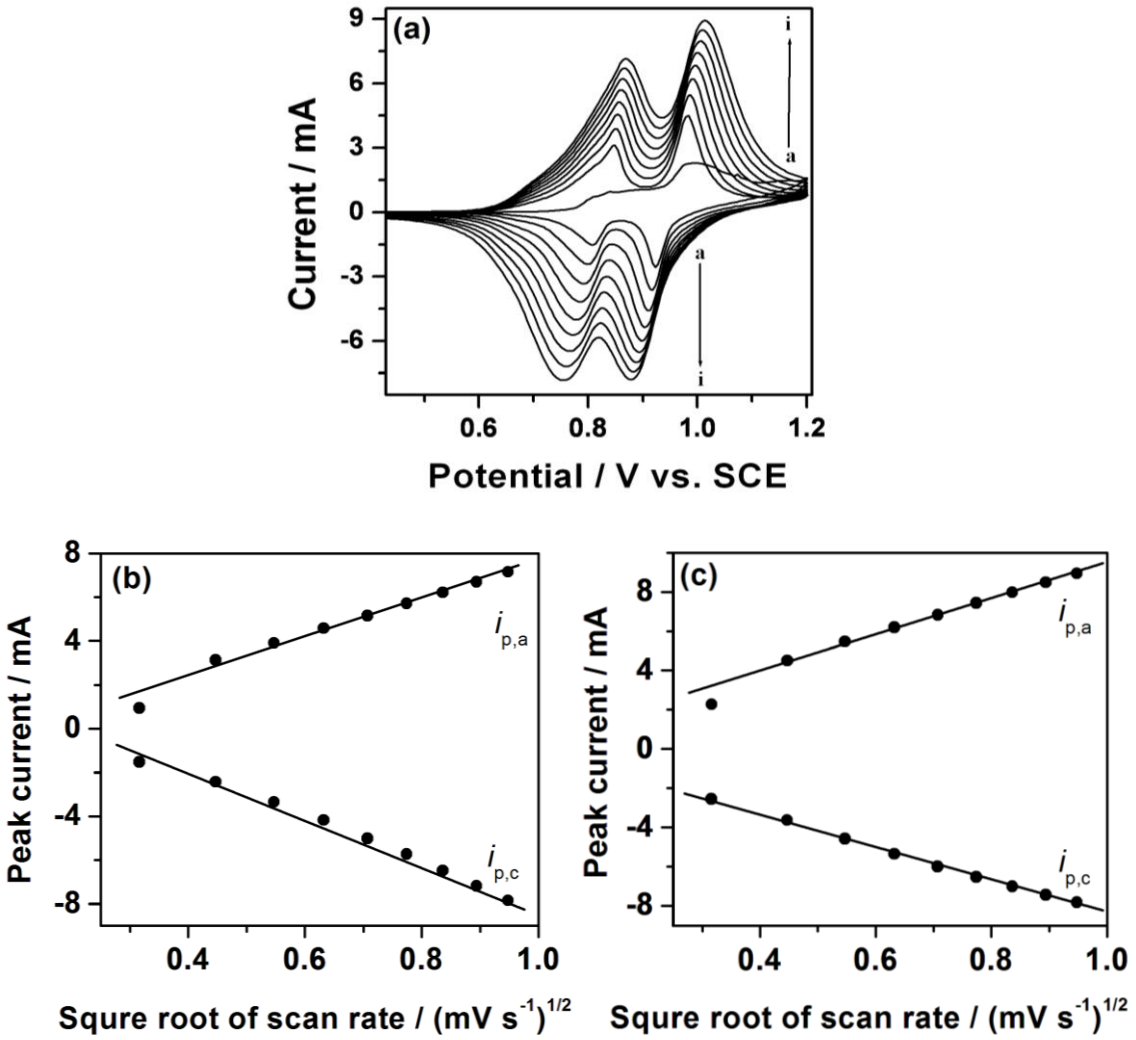

Figure 4: (a) CV of 5 wt. % graphene – $LiMn_2O_4$ composite electrodes in 5 M $LiNO_3$ at different scan rates from 0.1 to 0.9 mVs^{-1}. (b) and (c) Relationship between the peak currents and square root of scan rates for first and second peak pairs respectively.

Figure 4a shows the cyclic voltammograms of 5 wt. % graphene – $LiMn_2O_4$ composite electrode in 5 M $LiNO_3$ electrolyte obtained at different scan rates from 0.1 to 0.9 mVs^{-1}. The relationship between the peak currents ($i_{p,a}$ and $i_{p,c}$) and square root of scan rate ($v^{1/2}$) for anodic and cathodic peaks calculated from Figure 4a is as shown in **Figures 4b** and **4c**. The peak currents are proportional to $v^{1/2}$ at different scan rates. This shows that the lithium-ion de-intercalation/intercalation process taking place at the electrode is diffusion-controlled process. At lower scan rates, the system yielded almost reversible waves while at higher scan rates irreversible behavior was observed.

Table 4. Peak potential differences calculated from Figure 4a for 5 wt. % graphene – $LiMn_2O_4$ composite electrodes at different scan rates from 0.1 to 0.9 mV s^{-1}.

Scan rate (mVs^{-1})	$E_{p,a}$ (V) *Peak 1*	$E_{p,c}$ (V) *Peak 1*	$E_{p,a} - E_{p,c}$ (V) *Peak 1*	$E_{p,a}$ (V) *Peak 2*	$E_{p,c}$ (V) *Peak 2*	$E_{p,a} - E_{p,c}$ (V) *Peak 2*
0.1	0.843	0.808	0.035	0.998	0.923	0.075
0.2	0.848	0.798	0.050	0.983	0.918	0.065
0.3	0.852	0.793	0.059	0.987	0.908	0.079
0.4	0.853	0.788	0.065	0.988	0.903	0.085
0.5	0.858	0.778	0.080	0.993	0.898	0.095
0.6	0.858	0.773	0.085	0.998	0.893	0.105
0.7	0.863	0.768	0.095	1.003	0.888	0.115
0.8	0.868	0.758	0.110	1.008	0.883	0.125
0.9	0.868	0.753	0.115	1.013	0.878	0.135

Table 4 shows the peak potential difference values at different scan rates for 5 wt. % graphene – $LiMn_2O_4$ composite electrode. It can be observed that the peak potential difference between the two peaks is increased with increase in scan rate, although, the curve shapes of the anodic and cathodic peaks was almost symmetrical. From this observation we can infer that the reversibility of lithium-ion intercalation-deintercalation depends on scan rate, which may make us assume that the electrochemical lithium ion deintercalation-intercalation process changes from being kinetically quasi-reversible to irreversible when scan rate increases from low to high. Furthermore, the lithium ions cannot completely extract/insert from/into the bulk of the electrode during the time interval of a high scan rate.

To identify whether the cation deintercalated/intercalated from/into the electrode is lithium ion or not, we have recorded the CVs of the composite electrode at different concentrations of $LiNO_3$ aqueous electrolytes. **Figure 5a** shows the cyclic voltammograms of 5 wt. % graphene – $LiMn_2O_4$ composite electrode with a scan rate of 0.5 mV s^{-1} in various concentrations of $LiNO_3$ aqueous electrolytes. **Figure 5b** shows the plot of formal potential, $E_f = (E_{p,a} + E_{p,c})/2$ versus log $[Li^+]$ at various concentrations of alkali electrolyte solutions. The straight line with a positive slope confirms that, the redox peaks on the CVs in the $LiNO_3$ aqueous electrolytes can be attributed to the deintercalation-intercalation of lithium ions. In accordance with the reactions represented by Eq. 1 and 2 one should observe a linear relationship between the formal potential and activity of the lithium ion, according to Nernst equation ($E_f = E° + \log a_{Li+}$, i.e., the formal potential of the redox reaction should be directly proportional to the logarithm of lithium-ion activity in the $LiNO_3$ electrolyte solution).

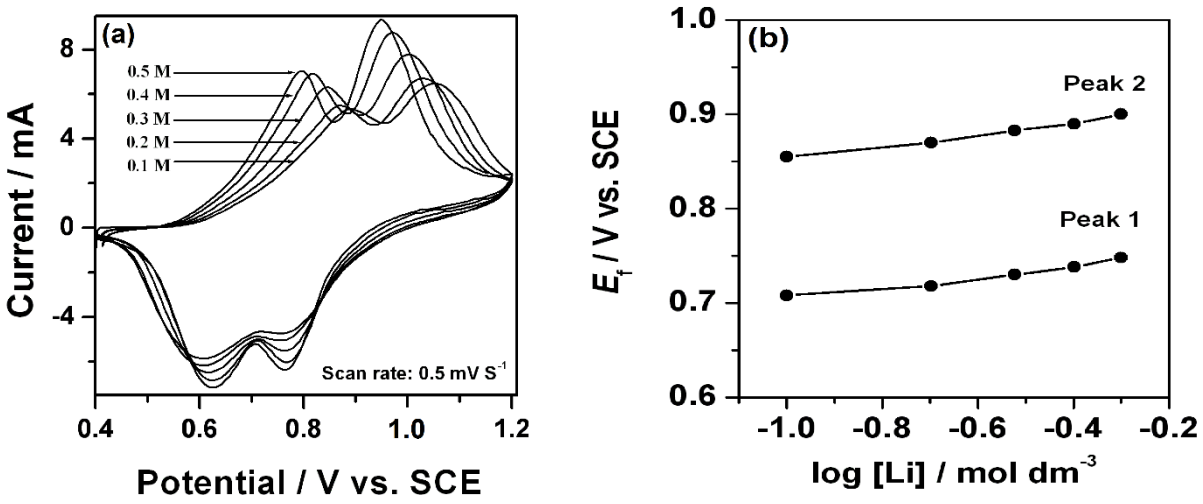

Figure 5: (a) CV of 5 wt. % graphene – $LiMn_2O_4$ composite electrode at a scan rate of 0.5 mVs^{-1} at different concentrations of $LiNO_3$ electrolyte. (b) Plot of E_f vs. log [Li^+] in $LiNO_3$ electrolytes at different concentrations.

3.3 Galvanostatic charge-discharge cycling.

To study the charge-discharge cycling behavior of the prepared composite electrode, an electrochemical cell was constructed using the 5 wt. % graphene–$LiMn_2O_4$ composite electrode as cathode and $LiTi_2(PO_4)_3$ as anode in 5 M $LiNO_3$ aqueous solution. The charge and discharge curves of $LiTi_2(PO_4)_3$ / 5 M $LiNO_3$ / graphene–$LiMn_2O_4$ composite cell at a current density of 0.1 mA cm^{-2} are shown in **Figure 6a**. It is clear that lithium ions deintercalate from $LiMn_2O_4$ and intercalate into $LiTi_2(PO_4)_3$ during the charge process and during discharge the opposite process occurs, i.e., lithium ions deintercalate from $LiTi_2(PO_4)_3$ and intercalate into $LiMn_2O_4$ in accordance with the following equations:

$$\text{Charge: } LiMn_2O_4 + LiTi_2(PO_4)_3 \rightarrow Li_{(1-x)}Mn_2O_4 + Li_{(1+x)}Ti_2(PO_4)_3 \quad (3)$$

$$\text{Discharge: } Li_{(1-x)}Mn_2O_4 + Li_{(1+x)}Ti_2(PO_4)_3 \rightarrow LiMn_2O_4 + LiTi_2(PO_4)_3 \quad (4)$$

It can be seen that two distinct plateaus appear on the charge curve as well as on the discharge curve, which corresponds, to the two-staged lithium deintercalation-intercalation behavior. For the charge process they locate at the potentials about 0.84 V and 0.97 V and for discharge process, they appear at 0.84 V and 0.71 V respectively. The two plateaus correspond to the two pairs of redox peaks on the cyclic voltammogram curve in Figure 2. In the first cycle, the specific capacity is about 100 mAh g^{-1} at a current density of 0.1 mA cm^{-2}. These curves are almost similar in shape and diplay an average voltage plateau of about 0.85 V. The pristine $LiMn_2O_4$ delivered an initial capacity of 90 mAh g^{-1}. The variation of discharge capacity with cycle number for both pristine and graphene composite $LiMn_2O_4$ electrodes is shown in **Figure 6b**. It can be observed that for pristine $LiMn_2O_4$ electrode capacity fades quickly as compared to that of the composite electrode. This can be ascribed to the good stability of the composite electrode during cycling in the aqueous electrolyte and shows that this kind of cell is good in reversible intercalation and deintercalation of lithium ions. Graphene addition improves the electrical conductivity of the composite electrodes and increases the utilization of $LiMn_2O_4$ by inducing an enhanced specific capacity. The 5 wt. % graphene–$LiMn_2O_4$ composite electrode exhibits better rate capability and high performance. Such an enhancement in the capacity

(about 10 mAh g^{-1}) is reported in literature upon coating polypyrrole [30] and polyaniline [31] for $Li_xV_2O_5$ anode material.

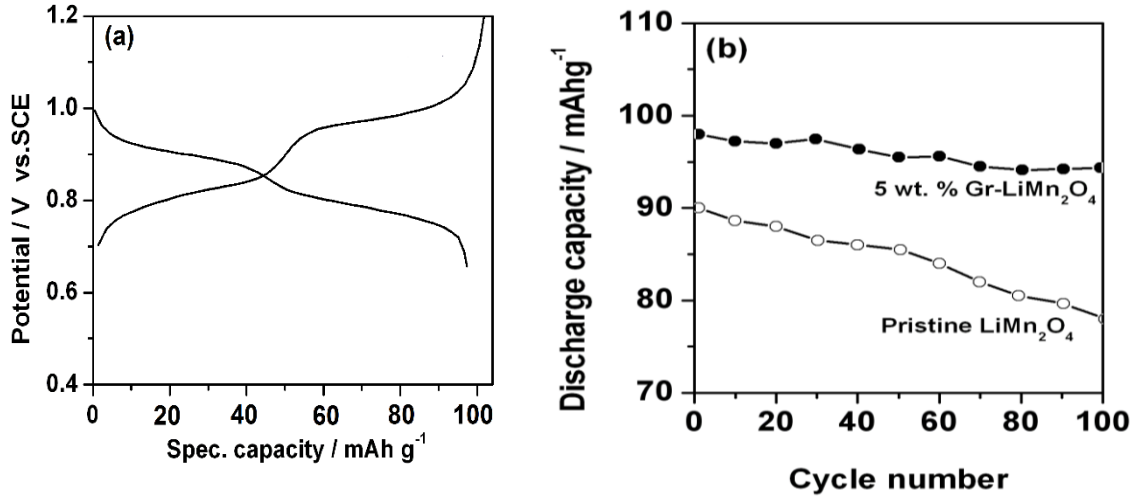

Figure 6: (a) Charge-discharge curves (b) cycling behavior at a current density of 0.1 mA cm^{-2} of $LiTi_2(PO_4)_3$ / 5 M $LiNO_3$ / 5 wt. % graphene–$LiMn_2O_4$ composite cell in 5 M $LiNO_3$ electrolyte (cycling behavior of pristine $LiMn_2O_4$ electrode is also shown for comparison).

The decrease in the capacity of higher weight percentage of graphene added composite electrodes can be explained as follows. With an increase in the amount of graphene in the composite, more amount of graphene is present between $LiMn_2O_4$ particles resulting in increased graphene material thickness between the active material particles. Hence, the utilization of graphene will decrease with an increase in graphene in the composite. Its specific capacity decreases due to less utilization of graphene as its amount increases. Based on the specific capacity, and utilization of graphene in the composites, it can be concluded that 5 wt.% represents an optimal amount of graphene in the composite or the extra addition (7.5 and 10 wt.%) of graphene may just add to the dead mass of the electrode which results in the decreased capacity of the cell.

3.4 Electrochemical impedance studies.

Electrochemical impedance spectroscopy was used to investigate the effect of graphene content on the lithium-ion transfer reaction kinetics in graphene-$LiMn_2O_4$ composite electrodes. Before taking the impedance spectra, the electrodes were cycled galvanostatically for few cycles to make sure if any formation of the stable SEI layer on the surface of the electrode. **Figure 7** shows Nyquist plots of untreated and graphene-$LiMn_2O_4$ composites in the lithiated state. The spectra show an intercept at high frequency region, a depressed semicircle in the high to middle frequency range, a Warburg type element in the low frequency range and a capacitive line. The intercept of impedance plot on the Z′ axis represents the ohmic resistance of the electrolyte.

The high frequency semicircle is related to the charge-transfer through the electrode–electrolyte interface, the Warburg region is assigned to solid state diffusion of lithium ions through the solid matrix of the cathode material. It can be observed from the figure that the semicircle becomes more suppressed in 5 wt. % graphene modified electrode. Decreased

diameter of the semicircle and the minimum of the semicircles when all the values of –Z″ are related indicates the improved charge transfer process at 5 wt. % graphene electrodes. Ohmic resistances of graphene-treated electrodes were smaller than that of the untreated $LiMn_2O_4$ suggesting a reduced resistance between electrolyte and electrode due to the addition of graphene to $LiMn_2O_4$.

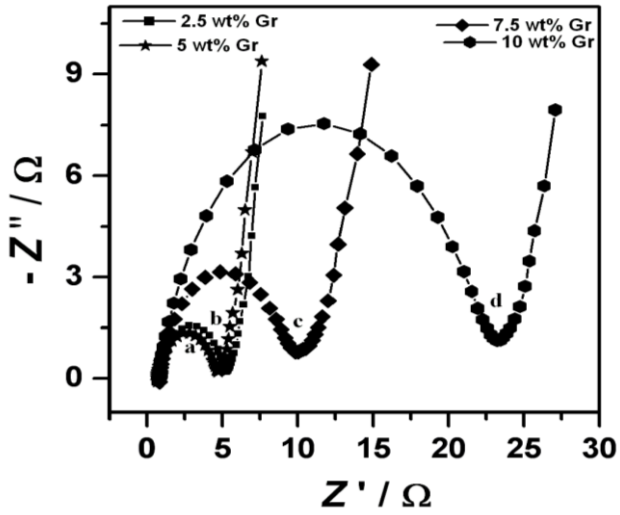

Figure 7: Nyquist plots of pristine and graphene-treated electrode in the fully lithiated state.

4. Conclusions

$LiMn_2O_4$ cathode material was successfully prepared by RAPET method. Addition of graphene is an effective way to improve the electrochemical properties of $LiMn_2O_4$ cathode material. Graphene could enhance the conductivity of $LiMn_2O_4$ material and produce good electrical contact between the particles. Cyclic voltammetry, galvanostatic charge-discharge experiments and electrochemical impedance studies provide strong evidence for improved reaction reversibility of $LiMn_2O_4$ cathode with graphene addition. 5 wt. % graphene has better electrochemical performance than 2.5, 7.5, and 10 wt. % graphene modified $LiMn_2O_4$ composite electrodes. The cell with 5 wt. % graphene-added cathode shows significant improvement in the electrochemical performance compared with that having pristine cathode. The drastic decrease in the charge transfer resistance obtained from EIS technique during lithium intercalation process for 5 wt. % graphene – $LiMn_2O_4$ compared to that for pristine $LiMn_2O_4$ proves that the enhanced charge transfer kinetics results from the addition of conductive and chemically stable graphene to $LiMn_2O_4$ cathode material.

Acknowledgement

The authors gratefully acknowledge the financial support from the Science and Engineering Research Board, New Delhi. The most important influence on the successful completion of this work was Dr. Sr. Sajitha, Campus coordinator, Mount Carmel College, Autonomous, Bengaluru, and we thank for her warm encouragement and understanding. Authors wish to thank Sri. A. V. S. Murthy, honorary secretary, Rashtreeya Sikshana Samiti Trust, Bengaluru, for his support. We gratefully acknowledge the encouragement from the management and staff of Mount Carmel College, Autonomous, Bengaluru.

References

1. K.S. Lee, S.T. Myung, H.J. Bang, S. Chung, and Y.K. Sun, *Electrochim. Acta*, **52**, 5201 (2007).
2. M.S. Whittingham, *Chem. Rev*., **104**, 4271 (2004).
3. R.J. Gummow, A. de Kock, and M.M. Thackeray, *Solid State Ionics*, **69**, 59 (1994).
4. D.H. Jang, Y.J. Shin, and S.M. Oh, *J. Electrochem. Soc*., **143**, 2204 (1996).
5. M.M. Thackeray, Y Shao-Horn, and A.J. Kahaian, *Electrochem. Soc. Interface*, **1**, 7 (1998).
6. P. Arora, B.N. Popov, R.E. White, *J. Electrochem. Soc*., **145**, 1998, 807.
7. J.M. Tarascon, W.R. Mckinnon, F. Coowar, T.N. Bowmer, G. Amatucci, and D. Goymard, *J. Electrochem. Soc*., **141**, 1421(1994).
8. S.-T Myung, H.-T Chung, S. Komaba, N. Kumagai, and H.-B. Gu, *J. Power Sources*, **90**, 103 (2000).
9. I.H. Kwon and M.Y. Song, *Solid State Ionics*, **158**, 103 (2003).
10. I. Taniguchi, D. Song, and M. Wakihara, *J. Power Sources*, **109**, 333 (2002).
11. Y.-C. Su, Q.-F. Zou, Y.-W. Wang, P.Yu, and J.-Y. Liu, *Mater. Chem. Phys*., **84**, 302 (2004).
12. B.-H. Kim, Y.-K. Choi, and Y.-H. Choa, *Solid State Ionics*, **158**, 281(2003).
13. C. Julien, S. Ziolkiewicz, M. Lemal, and M. Massot, *J. Mater. Chem*., **11**, 1837 (2001).
14. B. Deng, H. Nakamura, Q. Zhang, M. Yoshio, and Y. Xia, *Electrochim. Acta*, **49**, 1823 (2004).
15. L.W. Shacklette, T.R. Jow, M. Maxfield, and R. Hatami, *Synth. Metals*, **28**, C655 (1989).
16. M.G. Kanatzidis, *Chem. Eng. News*, **68**, 36 (1990).
17. H. Wang, H. S. Casalongue, Y. Liang, and H. Dai, *J. Am. Chem.Soc.*, **132**, 7472 (2010).
18. H. Wang, L. Cui, Y. Yang, H. S. Casalongue, J. T. Robinson, Y. Liang, Y. Cui, and H. Dai, *J. Am. Chem. Soc.*, **132**, 13978 (2010).
19. S. Yang, G. Cui, S. Pang, Q. Cao, U. Kolb, X. Feng, J. Maier, and K. Mullen, *Chem. Sus. Chem.*, **3**, 236 (2010).
20. S.L. Chou, J.Z. Wang, M. Choucair, H.K. Liu, J.A. Stride, and S.X. Dou, *Electrochem. Commun.*, **12**, 1388 (2010).
21. S.M. Paek, E. Yoo, and I. Honma, *Nano Letters*, **9**, 1530 (2009).
22. S. Yang, X. Feng, S. Ivanovici, and K. Mullen, *Ang. Chem.*, **49**, 1433 (2010).
23. W. Cho, W. Ra, J. Shirakawa, M. Nakayama, and M. Wakihara, *J. Solid State Chem*., **179** 3534 (2006).
24. H. Manjunatha, G. S. Suresh, and T. V. Venkatesha, *J. Solid State Electrochem.*, **15**, 431 (2010).
25. M. Jayalakshmi, M. Mohan Rao, and F. Scholz, *Langmuir*, **19**, 8403 (2003).
26. Y.J. Lee, F. Wang, and C.P. Grey, *J. Am. Chem. Soc*., **120**, 12601 (1991).
27. Y. Xia and M. Yoshio, *J. Electrochem. Soc*., **143**, 825 (1996).
28. W.R. Mckinnon, R.R. Haering, *Modern Aspects of Electrochemistry*, vol. **15**, Plenum Press, New York (1983).
29. D. Lu, W. Li, X. Zuo, Z. Yuan, and Q. Huang, *J. Phys. Chem. C*, **111**, 12067 (2007).
30. H. Wang, Y. Zeng, K. Huang, S. Liu, and L. Chen, *Electrochim. Acta*, **52**, 5102 (2007).
31. H. Wang, K. Huang, Y. Zeng, F. Zhao, and L. Chen, *Electrochem. Solid-State Lett*. **10**, A199 (2007).